Optimization and Engineering (2026) 27:587–616
https://doi.org/10.1007/s11081-025-10026-9

RESEARCH ARTICLE

Working fluid screening for ORC-based Carnot batteries by deterministic global optimization of design and nominal operation

Jannik T. Lüthje[1] · Marco Langiu[1] · Alexander Mitsos[1,2,3]

Received: 15 November 2024 / Revised: 14 August 2025 / Accepted: 15 August 2025 /
Published online: 26 September 2025
© The Author(s) 2025

Abstract

The rising temporal mismatch between energy supply and demand increases the need for large-scale energy storage. Carnot batteries offer a location-independent energy storage option and rely on readily available components. However, the low round-trip efficiency is an issue. Also, Carnot batteries have many degrees of freedom, making their optimal design and operation challenging. Additionally, the process is highly dependent on the working fluids used for the charging and discharging process. We optimize the Carnot battery design and nominal operation, including the working fluid selection. We perform deterministic global optimization to maximize the round-trip efficiency. Extending our previous work, we formulate a hybrid mechanistic/data-driven model in reduced space. We propose a model formulation for the thermal energy storage that is tailored to our problem and demonstrate that it results in substantial computational savings. We also extend our previously used surrogate model training procedure, by choosing surrogate models based on their relaxation tightness, strongly improving worst-case computational performance. These model improvements allow us to screen working fluids for the charging and discharging process by enumeration, globally optimizing each flowsheet with MAiNGO v0.7.2. Optimal round-trip efficiencies vary between 30% and 60% and are typically found in the root node (multistart) but for some cases during branch-and-bound. However, the top working fluid combinations include fluids with a strong environmental impact, indicating the need to include environmental objectives.

Keywords Hybrid modeling · Pumped thermal energy storage · Artificial neural networks · Reduced space modeling · Deterministic global optimization · MAiNGO

✉ Alexander Mitsos
amitsos@alum.mit.edu

[1] Process Systems Engineering (AVT.SVT), RWTH Aachen University, Forckenbeckstr. 51, 52074 Aachen, Germany

[2] JARA-ENERGY, Templergraben 55, 52056 Aachen, Germany

[3] Institute of Climate and Energy Systems: Energy Systems Engineering (ICE-1), Forschungszentrum Jülich GmbH, 52425 Jülich, Germany

1 Introduction

The increasing fraction of renewable energy sources in the electricity mix, combined with the reduction of conventional base-load power plants, results in a growing need for electricity storage in the range of multiple hours to days (Cebulla et al. 2018). While various technologies are considered for such storage time frames, so-called Carnot batteries (CBs) are a particularly promising option due to their high energy density, location independence, and long lifetime. Several recent works reviewed different aspects of CBs (Dumont et al. 2020; Novotny et al. 2022; Vecchi et al. 2022; Liang et al. 2022; Ma et al. 2022). CBs provide energy storage for the electric grid in the required time range by combining three technologies: power to heat P2H, thermal energy storage (TES), and heat to power (H2P). During times of low electricity prices or high electricity availability, the P2H process is used to store electrical energy as thermal energy via transferring heat from a low-temperature TES to a high-temperature TES. When the electricity price increases or there is a low electricity availability, heat flows back from the high-temperature TES to the low-temperature TES via the H2P process which converts a part to electricity.

Although individually P2H, TES, and H2P are all well-established technology classes, the chosen technologies from each of the three technology classes need to be optimally adapted to each other to ensure economic feasibility. Two major options are available for the TES (Liang et al. 2022). So-called "sensible" TES utilize a storage medium that changes its temperature depending on the amount of thermal energy stored (e.g., pressurized water). In the "latent" TES, storage is based on phase-change material (PCM), and thus the temperature remains mostly constant over the entire operating range. Different storage concepts can also be combined, e.g., proposed by Palacios et al. (2020). For charging, several planned and existing grid-scale CB projects use electric heaters (Novotny et al. 2022; Vecchi et al. 2022), as they are simple, cheap, allow for fast response times, and enable high storage temperatures, improving the possibility of high discharge efficiencies. However, direct electrical heating is exergetically disadvantageous, as heat is exclusively obtained from the conversion of electricity. Hence, the ratio of usable heat to input power is at most one. Alternative CBs variants, also called pumped thermal energy storage (PTES), use heat pumps (HPs), which generally have higher heat-to-power ratios, and thus enable overall round-trip efficiencies (RTEs) above the efficiency of the chosen H2P technology. The RTE is defined as the ratio of the total released electricity during the entire discharging process to the total absorbed electricity during the charging process.

PTES can be classified depending on the thermodynamic states the working fluid (WF) experiences during the cycle. Brayton-based PTES systems use a reverse Brayton cycle as a HP for charging and a standard Brayton cycle for discharging. To ensure small temperature differences during heat transfer, they are typically combined with a high-temperature sensible TES, most commonly with direct heat transfer from the gaseous WF to packed beds (Dumont et al. 2020). This class of CBs draws its advantages from the mature technology of gas turbines, allowing for large temperature ratios, enabling a high RTE and storage density. However, with the temperature ratio, the pressure ratio also increases, resulting in a pressurized (and thus more costly) hot storage in the case of direct contact of WF and storage medium. This can be partly mitigated by

using mono-atomic gases as WFs (White et al. 2013). While theoretical works predict high RTEs above 70% (Desrues et al. 2010; McTigue et al. 2015; Laughlin 2017), a major limitation is the maximum compressor operating temperature of about 500°C (Dumont et al. 2020). High compressor efficiencies (> 90%) can, however, still lead to high RTEs (Desrues et al. 2010). Higher operating temperatures may be achieved by combining a reverse Brayton cycle with an electrical heater (Benato and Stoppato 2018).

Supercritical cycles operate in the regime of supercritical fluids, i.e., above critical pressure, during the entire cycle and are most similar to Brayton-based cycles. PTES concepts based on these types of cycles frequently use CO_2 as a WF, as it has a reduced susceptibility to isentropic efficiencies of the rotating equipment (McTigue et al. 2020).

The third class of PTES uses a vapor-compression HP for charging and a Rankine cycle for discharging. In general, these cycles require smaller mass and volume flows, compared to Brayton-based PTES (Steinmann 2014) and benefit from the fact that pumps are used instead of compressors in the discharge cycle, as the WF is a liquid after leaving the condenser (i.e., the low-temperature TES). A subclass of Rankine-based CBs are Organic Rankine cycle (ORC)-based CBs, for which a wide variety of alternative WFs are considered, several of which are already in industrial use, as refrigerants or in power applications such as geothermal plants and waste heat recovery. Isentropic WFs (i.e., nearly vertical slope of the saturated vapor line in the T-s diagram) are of particular interest for ORC-based PTES as they do not require superheating in charging or discharging mode (Hassan et al. 2020). Due to the lower temperatures, ORC-based PTES generally achieve smaller power outputs, with maximum values in the range of 10 MW to 100 MW (Novotny et al. 2022; Vecchi et al. 2022).

Several other CBs concepts have been proposed. These include transcritical cycles and cryogenic or adsorption-based PTES. All CBs variants can achieve only limited RTEs due to efficiency losses in the charging and discharging process. An option to improve the RTE without improving the charging/discharging efficiency is the use of low-temperature waste heat streams for charging. This can result in a RTE $\geq$ 100% (Jockenhöfer et al. 2018). Other options to improve RTE include internal heat regeneration, multiple expansion (and compression) stages, multiple storage tanks, or WF mixtures (e.g., Steinmann 2014; Sanz Garcia et al. 2019).

The WF properties have a large effect on all of the listed variants. In Liang et al. (2022), WF selection is identified as one of the key influences on CBs performance. For ORCs, WF selection has also been thoroughly investigated (e.g., Bao and Zhao 2013; Huster et al. 2020b, d). This investigation also included WF mixtures. For CBs, Koen et al. (2021) investigated a WF mixture consisting of four different alkanes, achieving a RTE of over 50% while utilizing storage temperatures under 100°C. However, most of CBs literature focuses on pure WFs.

Summing up, many different CB configurations are proposed in the literature. Choosing the best option for each of the three technology types together with the optimal WF (i.e., optimizing the CB design) is still an open research question, as the optimal P2H process, TES, H2P process, and WFs all depend on each other. For this, a model of the CB, to embed into the optimization problem, is required. This optimization problem will be nonlinear and nonconvex due to accurate thermodynamic

relations of the CB model. The optimization problem can be solved via local, stochastic global, or deterministic global solvers (Locatelli and Schoen 2013). Only deterministic global solvers can guarantee finding the best possible solution. Local solvers can get stuck in local minima, while global stochastic solvers cannot give a guarantee for optimality. Therefore, deterministic global optimization (DGO) is preferable for the comparison of different CB designs or WFs. To our knowledge, no work on DGO of CB design has been published so far.

Morandin et al. (2013) use a genetic algorithm (GA) for determining the system structure of a transcritical CO_2-based CB, capable of supplying 50 MWe of power over 2 h, and a nested linear programming subroutine for determining the required sizes of the charging machinery. Fan and Xi (2022) extend the scope of optimization to the selection of CB technology and WF using a GA to optimize the levelized cost of storage (LCOS), RTE and exergy efficiency as objective functions. Eppinger et al. (2020) simulate the influence of WF and type of storage on the CB RTE. However, they do not optimize. Tillmanns et al. (2022) perform a thermo-economic optimization of a ORC-based CB, including the WF selection. Frate et al. (2020) investigate 8 different WFs for a CB that utilizes a waste heat stream. Also, they consider the use of recuperators.

Process models require accurate thermodynamic relations, especially when the influence of the WF needs to be investigated. While thermodynamic libraries such as CoolProp (Bell et al. 2014) or REFPROP (Lemmon et al. 2018) exist, they cannot directly be integrated into models for global deterministic optimization due to their black-box nature. To deal with this issue, we have proposed a framework in which the thermodynamic libraries are used to generate data, on which surrogate models are trained, which can then be integrated into the process model (Schweidtmann et al. 2019). Integrating the surrogate models into the optimization problem is handled by our open-source MeLOn toolbox (Schweidtmann et al. 2020). Combining mechanistic model equations with data-driven sub-models results in a so-called *hybrid model* (Psichogios and Ungar 1992; Kahrs and Marquardt 2007). This approach enables us to formulate the problem in reduced space (RS), strongly improving computational performance. In later publications, we used this method for the optimization of various aspects of ORCs, including the WF screening (Huster et al. 2020a, b, c, d). Many other groups have published work on hybrid modeling for process optimization. For comprehensive reviews on hybrid modeling, we refer the readers to McBride and Sundmacher (2019); Bradley et al. (2022); Pistikopoulos and Tian (2024). Asprion et al. (2019) consider using surrogate models to optimize a large process flowsheet where no model is available for some process units. Winz et al. (2021) replace expensive equilibrium calculations with surrogate models for process optimization. Ceccon et al. (2022) propose a framework which allows the inclusion of (ANNs) and gradient-boosted trees in optimization problems. Zhang et al. (2024) extend this framework with the ability to solve optimization problems with Graph Neural Networks (GNNs) embedded.

In this work, we extend our previous framework for the WF screening for ORCs to CBs. For this, we consider pure, but possibly different, WFs for the P2H and H2P process. We focus on ORC-based CBs as the required equipment is already technically mature (Dumont et al. 2020). Since a big advantage of CBs is location independence, we do not consider the use of a waste heat stream for charging. For

improved efficiency, we consider using a recuperator for both HP and ORC. We aim to establish a computationally feasible model formulation that allows us to screen the RTE of a large number of WF combinations by DGO. For this, we develop a reduced-space formulation of the TES. The core concept behind this approach is that, in the given optimization problem, the TES temperatures do not directly impact the objective function. Their role is solely to ensure the feasibility of heat transfer between HP and TES and between TES and ORC. Therefore, we eliminate them from the set of optimization variables and introduce constraints, guaranteeing the existence of feasible TES temperatures that maintain a minimum temperature difference at the pinch. Additionally, we propose an improvement to the previously used ANN training procedure that aims to generate ANNs that are especially suited to DGO. For the optimization, we use the parallel version of our open-source global deterministic solver MAiNGO (Bongartz et al. 2018).

The remainder of this article is structured as follows. First, we briefly describe the CB process in Sect. 2. We then explain our modeling approach in Sect. 3. Next, we detail the training of the thermodynamic surrogate models and the RS formulation of the CB in Sect. 4. Implementation details are given in Sect. 5. Afterward, we analyze the results of the WF screening in Sect. 6 and comment on the computational performance. Finally, we summarize the paper and provide an outlook in Sect. 7.

2 ORC-based Carnot battery

A flowsheet of the investigated CB structure is shown in Fig. 1. We consider a CB, which uses the environment as the low-temperature TES as such a layout reduces capital cost compared to a two-storage solution. Thus, the evaporator of the HP and the condenser of the ORC are connected to the environment. For this work, we do not specify the mechanism of this heat transfer (e.g., via air or cooling water). Instead, we later assume a representative environmental temperature to which we ensure a minimum temperature difference. Additionally, we neglect parasitic losses that might occur due to the heat transfer to/from the environment. Exemplary T-s-diagrams are presented in Fig. 2. For the charging process (Fig. 1a and Fig. 2a), a HP with a recuperator is used. The WF exits the ambient heat exchanger as a saturated vapor (1a). It is then preheated in the recuperator (1a → 2a). In the compressor, the pressure is increased from the low pressure level $p_{\mathrm{L}}^{\mathrm{HP}}$ to the high pressure level $p_{\mathrm{H}}^{\mathrm{HP}}$ (2a → 3a). In- and outlet of the compressor lie in the vapor region. The fluid then enters the heat exchanger to the hot storage, where it is cooled down to saturation temperature (3a → 3a'), condensed (3a' → 3a''), and subcooled (3a'' → 4a). The fluid is then further subcooled in the recuperator (4a → 5a). Afterward, a valve expands the fluid into the two-phase state (5a → 6a). To close the cycle, the ambient heat exchanger fully evaporates the two-phase flow (6a → 1a).

For the discharging process, an ORC with recuperator (Fig. 1b and Fig. 2b) is operated. The WF leaves the ambient heat exchanger as a saturated liquid (1b). This liquid is then pumped up from the low pressure level $p_{\mathrm{L}}^{\mathrm{ORC}}$ to the high pressure level $p_{\mathrm{H}}^{\mathrm{ORC}}$ (1b → 2b). Afterwards, the fluid is preheated in the recuperator (2b → 3b) before entering the hot storage. The fluid is brought up to saturation temperature (3b

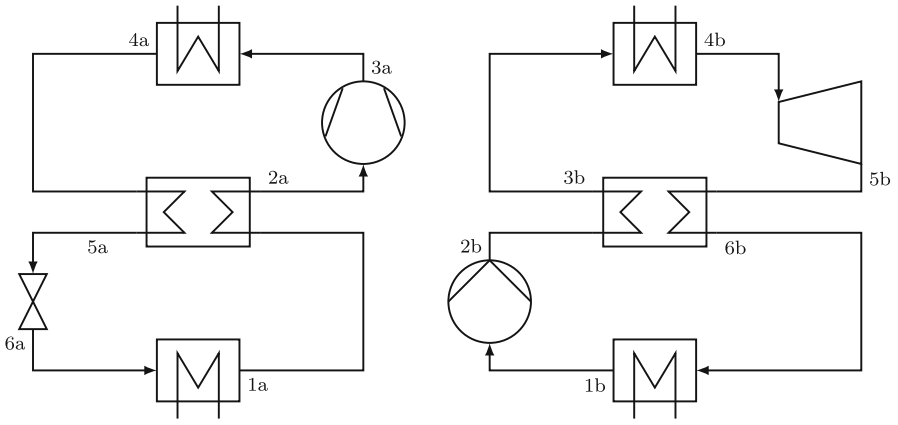

(a) Charging process (HP) (b) Discharging process (ORC)

Fig. 1 Flowsheet of the modeled CB

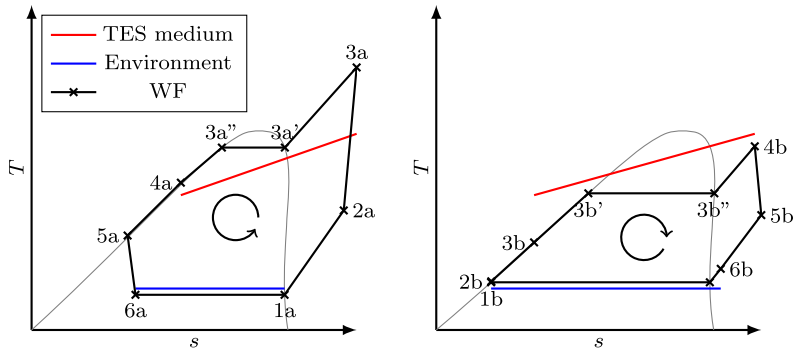

(a) Charging process (HP) (b) Discharging process (ORC)

Fig. 2 *T*-*s*-diagram of the modeled CB

→ 3b’), evaporated (3b’ → 3b”), and superheated (3b” → 4b) by the storage medium. The fluid is then relaxed in the turbine (4b → 5b). In- and outlet of the turbine are superheated vapors. Next, the fluid is cooled down in the recuperator (5b → 6b). Finally, the fluid is condensed in the ambient heat exchanger (6b → 1b).

3 Model

We aim to screen possible WF candidates for HP and ORC according to the RTE that the optimal CB with these WFs can achieve. Therefore, equipment sizing and capital costs are not of interest and are thus not included in the model. To calculate the RTE, we assume that the CB has an equal charging and discharging time during nominal operation (i.e., the heat flow from HP to TES is equal to the heat flow from TES to ORC and there is no heat transfer from the TES to the environment). Doing so, we can

Table 1 Overview of trained ANNs for a single WF

Phase	Inputs	Output
Vapor	p, h	T
	p, h	s
	p, s	h
Liquid	p, h	T
	p, s	h
Saturated	p	T
	p	h'
	p	h''
	p	s'

define the RTE as a power ratio instead of an energy ratio. This allows us to skip the relative sizing of HP and ORC as optimization variables in the optimization problem. Thus, we calculate the RTE ϵ as the ratio of the nominal ORC power ($P_{\text{turb}}^{\text{ORC}} - P_{\text{pump}}^{\text{ORC}}$) to the HP compressor power ($P_{\text{comp}}^{\text{HP}}$):

$$\epsilon = \frac{P_{\text{turb}}^{\text{ORC}} - P_{\text{pump}}^{\text{ORC}}}{P_{\text{comp}}^{\text{HP}}} = COP^{\text{HP}} \eta^{\text{ORC}} \tag{1}$$

3.1 Working fluid

We consider pure WFs for HP and ORC. We allow for WF combinations that use the same WF for HP and ORC. Following the approach in Schweidtmann et al. (2019), we model the WFs via ANNs that are trained on data from a thermophysical property database. While the underlying data is generated using an equation of state (EoS), which is explicit only for density and temperature, we train ANNs for every combination of inputs that are required by the CB model. This results in explicit expressions for all required thermodynamic relations, which was shown to lead to significant computational savings compared to the use of implicit expressions (Schweidtmann et al. 2019). We train an individual ANN for every combination of inputs, output, phase, and WF. We then directly include these ANNs in the model formulation. For example, we calculate the temperature of gaseous isobutene as a function of pressure and enthalpy as:

$$T = f_{\text{vap},(p,h)\rightarrow T}^{\text{ANN,Isobutene}}(p, h). \tag{2}$$

This results in 9 different ANNs for each WF as shown in Table 1. In Section 4, we provide details regarding the training and data generation procedure.

3.2 Rotating machinery

We model the rotating equipment via isentropic efficiencies, which we assume to be constant. First, we calculate the isentropic reference state $h_{\text{out}}^{\text{is}}$ for the considered state and WF based on the output pressure p_{out} and inlet entropy s_{in}:

$$h_{\text{out}}^{\text{is}} = f_{<\text{state}>,(p,s)\rightarrow h}^{\text{ANN},<\text{WF}>}(p_{\text{out}}, s_{\text{in}}) \tag{3}$$

Then, we calculate the real output $h_{\text{out}}^{\text{real}}$ based on the inlet enthalpy h_{in}, the isentropic reference state, and the isentropic efficiency η^{is}. For the compressor and pump, this results in

$$h_{\text{out}}^{\text{real}} = h_{\text{in}} + \frac{h_{\text{out}}^{\text{is}} - h_{\text{in}}}{\eta_{\text{pump/comp}}^{\text{is}}}, \tag{4}$$

and for the turbine in

$$h_{\text{out}}^{\text{real}} = h_{\text{in}} + \eta_{\text{turb}}^{\text{is}}(h_{\text{out}}^{\text{is}} - h_{\text{in}}). \tag{5}$$

3.3 Recuperator

We model the recuperator via an enthalpy balance, assuming no heat transfer to the environment. We further assume that the pinch can only occur at either the in- or outlet of the recuperator. To ensure the minimum temperature difference $\Delta T_{\text{min}}^{\text{recup}}$ at the in-/outlet we add inequality constraints:

$$T_{\text{out}}^{\text{cold}} + \Delta T_{\text{min}}^{\text{recup}} - T_{\text{in}}^{\text{hot}} \leq 0 \tag{6}$$

$$T_{\text{in}}^{\text{cold}} + \Delta T_{\text{min}}^{\text{recup}} - T_{\text{out}}^{\text{hot}} \leq 0 \tag{7}$$

3.4 Thermal energy storage

For the TES we assume no heat transfer to the environment (i.e., no heat loss) and storage characteristics that are independent of the state of charge. For the storage medium, we assume either a PCM with an isothermal phase change or a fluid that exhibits a constant heat capacity over the considered operating range. This is equivalent to a straight line in the T-Q-diagram of the TES. We assume that the pinch occurs at either the in-/outlet of the TES or at the saturated states of the WFs. We ensure that at the pinch the minimum temperature difference $\Delta T_{\text{min}}^{\text{TES}}$ is not exceeded through the use of inequality constraints.

The storage medium determines the valid range of the storage temperature. However, we assume that suitable sensible storage media can always be found for any storage temperatures. This is motivated by the small temperature ranges of ORC-based CBs, compared to the large usable temperature ranges of sensible storage media (e.g., Therminol 66 supports a range from −3°C to 345°C, Liang et al. (2022)).

PCMs release/absorb heat at an almost constant phase change temperature, which is determined by the PCM. It follows that for latent storage, only discrete storage temperatures are available when using a pure PCM. However, mixing allows a continuous adjustment of phase change temperatures. E.g., Durth et al. (2019) show that a mixture of KNO_3 and $NaNO_3$ results in melting temperatures ranging from 220°C to 330°C. Thus, we assume that a matching PCM can be found or engineered for every desired latent storage temperature. Therefore, we consider no constraints on the storage temperature. From a DGO viewpoint, this assumption is a relaxation of a CB model that considers the storage medium selection problem.

4 Method

This section outlines the main components of our approach. We first perform a WF preselection to determine a set of WF candidates. Next, we generate thermodynamic data, which we later use in the custom ANN training loop. Following this, we introduce our tailored RS TES model formulation. Finally, we describe the full CB model, which we optimize subsequently. In Fig. 3 we show an overview of the proposed method.

4.1 Working fluid preselection

Similar to Huster et al. (2020d), we perform a WF preselection to exclude unsuitable fluids from the study. For this, we start with a list of all fluids that are available in the thermodynamic library. Since this work focuses on subcritical processes, we filter out all fluids with a critical pressure $p_{\text{crit}} \leq 10\,\text{bar}$ (Huster et al. 2019b). The equations the thermodynamic library uses to generate data are only valid for pressures larger than a fluid-dependent p_{min}. Thus, in the next step, we filter out WFs where $p_{\text{min}} \leq 0.2\,\text{bar}$. For the fluids that are removed in this step, we would not be able to

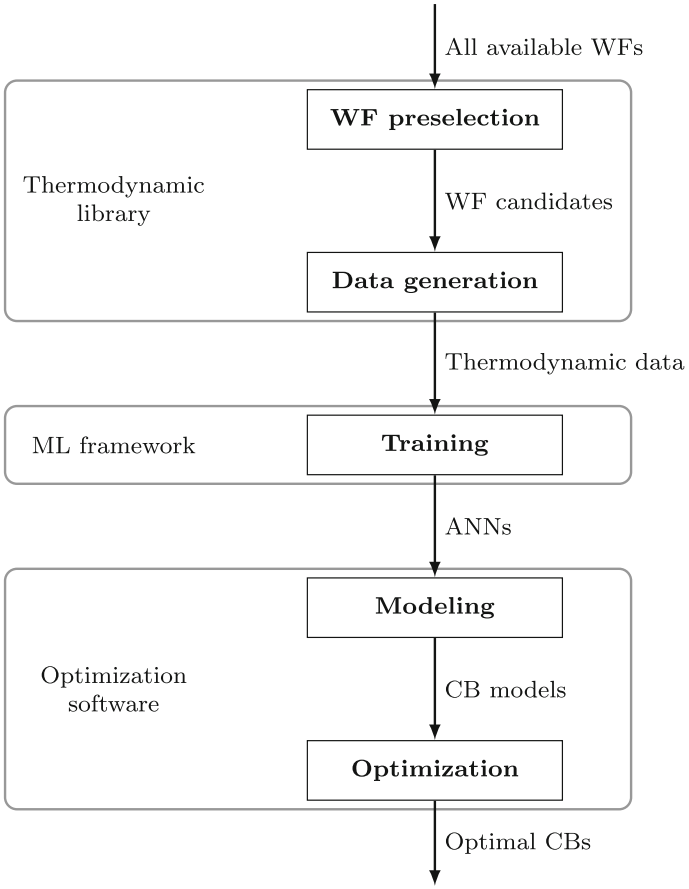

Fig. 3 Overview of the method proposed in this work with intermediate results and tools used. The individual steps are described in the following subsections

generate training data at low pressures. For the operation of the HP, the WF must be capable of condensing at the high pressure level, at a temperature above the ambient temperature. To ensure this, we screen all fluids based on the criterion:

$$T_{\text{sat}}\,(p = 10\,\text{bar}) \geq 323.15\,\text{K} \tag{8}$$

Additionally, at the low pressure level, the fluid must be evaporated at ambient temperatures, even during winter conditions:

$$T_{\text{sat}}\,(p = 0.2\,\text{bar}) \leq 258.15\,\text{K} \tag{9}$$

4.2 Data generation

After the WF preselection, we generate training data for each WF candidate. Following the approach of Schweidtmann and Mitsos (2018), we use latin hypercube sampling (LHS) to generate data points consisting of pressure and temperature. We apply the following bounds for the data generation:

$$T \in [250\,\mathrm{K}, 600\,\mathrm{K}] \tag{10}$$

$$p \in [0.1\,\mathrm{bar}, 0.9\,p_{\mathrm{crit}}] \tag{11}$$

Within these bounds, we create 10 000 data points. For every data point (p, T), we compare the temperature T against the saturation temperature $T_{\mathrm{sat}}(p)$. We build a liquid phase dataset from all points with $T \leq T_{\mathrm{sat}}(p)$. The remaining data points are used to assemble the vapor phase data set. We calculate enthalpy and entropy for every data point via the thermodynamic library.

For the saturated state, we consider 1000 pressures in $[0.1\,\mathrm{bar}, 0.9\,p_{\mathrm{crit}}]$. For every pressure, we calculate the enthalpy and the entropy of the saturated liquid and vapor state (h', h'', s', s'').

4.3 ANN training

We aim to train ANNs to a sufficient accuracy while still allowing for fast convergence of the process optimization. MAiNGO uses McCormick relaxations (McCormick 1976) to construct convex underestimators and concave overestimators of constraints and the objective. The tightness of these relaxations affects the computational performance of the DGO. Huster et al. (2019a) show that ANN size (i.e., number of neurons) has a large influence on the relaxation tightness. While the ANN accuracy improves with increasing ANN size, the relaxation tightness (and thus the computational performance) decreases. Thus, our training process aims to find the smallest possible ANNs that still reach appropriate accuracies. Additionally, due to the non-deterministic nature of the training process, each run produces a different ANN. Therefore, conducting multiple training runs may be advantageous. With these considerations, we arrive at the following training procedure:

Before training, we normalize the data to match better the input/output ranges of the chosen activation function (tanh). We normalize the inputs to the interval $[-1, 1]$ and the target output to a mean of 0 and a standard deviation of 1. We choose Levenberg-Marquardt (LM) as the training algorithm. Compared to the commonly-used first-order training methods (e.g., Adam), LM exhibits faster convergence, higher robustness, and achieves more accurate ANNs (Hagan and Menhaj 1994). This comes at a higher computational cost which is, however, neglible due to the small ANN sizes that we consider. Also, we deploy early stopping to prevent overfitting. As performance metric, we choose the mean squared error (MSE).

All ANNs are fully-connected with a single hidden layer. This simple architecture is sufficient since the ANNs are only used for a small part of our hybrid model (mapping of thermodynamic properties). The architecture of the resulting hybrid model is much

more complex. While the ANNs architecture is simple, it enables universal approximation and there are no spatial or temporal patterns in the thermodynamic data that could be exploited by a specialized architecture. Also, the low number of parameters compared to the size of the dataset makes overfitting unlikely. We iteratively determine the size of the hidden layer as described in the following. Initially, we set a target MSE for every ANN. We employ a custom training loop that, for each ANN which needs to be trained, starts at a small initial layer size (number of neurons). First, we train the ANN until either the maximum number of epochs is reached or the training is stopped due to early stopping. Then, we check whether the target MSE was reached. If this is not the case, we increase the layer size and restart the training. If the target MSE was reached, we save the ANN as a potential candidate. We repeat the procedure k-times, which results in a set of k ANNs candidates that all achieve the target MSE. For the results presented in this work, we use $k = 5$. Then, for each ANN, we compute the convex and concave McCormick relaxation over the entire input range. We evaluate the relaxations at $N = 100$ (if the ANN has 1 input) or $N = 400$ (for 2 inputs) points. We calculate a relaxation score as follows:

$$\text{score} = \frac{\sum_n^N \left(f_{\text{cc}}^{\text{ANN}}(\boldsymbol{x}_n) - f_{\text{cv}}^{\text{ANN}}(\boldsymbol{x}_n) \right)}{\sum_n^N f^{\text{ANN}}(\boldsymbol{x}_n)} \tag{12}$$

This score represents the average distance between concave and convex relaxation, normalized by the average ANN output, thus indicating the relaxation's tightness. We rank the k ANN candidates according to their relaxation score and choose the ANN with the tightest relaxations (i.e., the lowest score) to be included in the CB model for the subsequent process optimization.

4.4 TES model formulation

Due to assuming no heat transfer from the TES to the environment and equal nominal charging/discharging times, the heat flow between the TES and WF $\dot{Q}^{\text{TES}}$ is equal during charging and discharging:

$$\dot{m}^{\text{HP}} \left(h_{\text{in}}^{\text{HP}} - h_{\text{out}}^{\text{HP}} \right) = \dot{Q}^{\text{TES}} = \dot{m}^{\text{ORC}} \left(h_{\text{out}}^{\text{ORC}} - h_{\text{in}}^{\text{ORC}} \right) \tag{13}$$

Next, we must guarantee feasible heat transfer conditions by formulating inequality constraints that enforce the minimum temperature difference $\Delta T_{\text{min}}^{\text{TES}}$ in the TES. For this, we present two approaches. The first one is commonly used in literature but does not follow the RS modeling paradigm. The second approach is our proposed modeling approach that is tailored towards the CB model and exploits its assumptions. For the first approach (called T-approach from here on), two optimization variables describe the TES medium. As we assume a constant heat capacity for the medium, two variables are sufficient to describe the storage medium temperature profile for a given heat flow to/from the TES ($\dot{Q}^{\text{TES}}$). These variables could be the minimum and maximum storage temperature $T_{\text{min}}^{\text{TES}}$, $T_{\text{max}}^{\text{TES}}$ (e.g., Frate et al. 2020). Another option would be one TES temperature and the heat capacity rate $C^{\text{TES}} = \dot{m}^{\text{TES}} c_p^{\text{TES}}$ (i.e.,

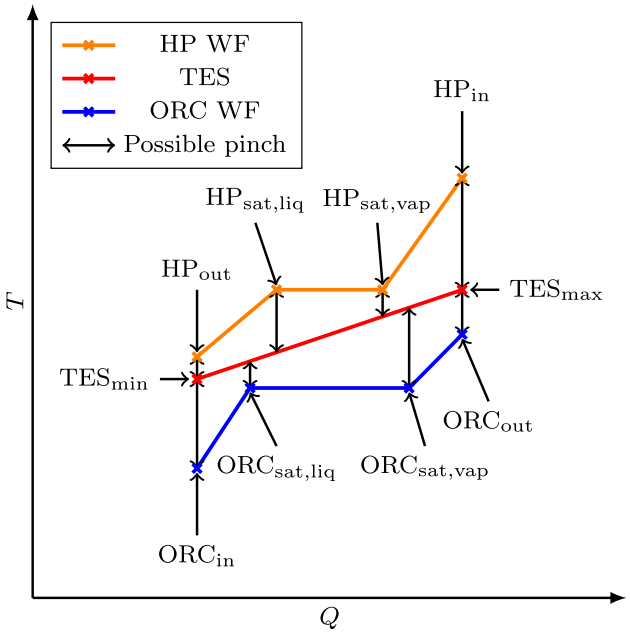

Fig. 4 T-Q-diagram for the TES

the slope of the TES in the T-Q-diagram). This option was used by Tillmanns et al. (2022). We implement the two-temperature variant for our TES model. However, both variants result in similar model equations. We show an exemplary T-Q-diagram in Fig. 4. Due to the assumptions taken in Sect. 3.4, the pinch between WF and TES can only be located at the TES in-/outlet or at the saturated WF states. To ensure the minimum temperature difference between HP and TES at the pinch point candidates, we add the following constraints:

$$T_{\text{min}}^{\text{TES}} + \Delta T_{\text{min}}^{\text{TES}} - T_{\text{out}}^{\text{HP}} \leq 0 \tag{14}$$

$$T_{\text{min}}^{\text{TES}} + \left(T_{\text{max}}^{\text{TES}} - T_{\text{min}}^{\text{TES}}\right) \frac{h_{\text{sat,liq}}^{\text{HP}} - h_{\text{out}}^{\text{HP}}}{h_{\text{in}}^{\text{HP}} - h_{\text{out}}^{\text{HP}}} + \Delta T_{\text{min}}^{\text{TES}} - T_{\text{sat}}^{\text{HP}} \leq 0 \tag{15}$$

$$T_{\text{min}}^{\text{TES}} + \left(T_{\text{max}}^{\text{TES}} - T_{\text{min}}^{\text{TES}}\right) \frac{h_{\text{sat,vap}}^{\text{HP}} - h_{\text{out}}^{\text{HP}}}{h_{\text{in}}^{\text{HP}} - h_{\text{out}}^{\text{HP}}} + \Delta T_{\text{min}}^{\text{TES}} - T_{\text{sat}}^{\text{HP}} \leq 0 \tag{16}$$

$$T_{\text{max}}^{\text{TES}} + \Delta T_{\text{min}}^{\text{TES}} - T_{\text{in}}^{\text{HP}} \leq 0 \tag{17}$$

For the heat exchange between TES and ORC, we formulate similar constraints:

$$T_{\text{in}}^{\text{ORC}} + \Delta T_{\text{min}}^{\text{TES}} - T_{\text{min}}^{\text{TES}} \leq 0 \tag{18}$$

$$T_{\text{sat}}^{\text{ORC}} + \Delta T_{\text{min}}^{\text{TES}} - \left(T_{\text{min}}^{\text{TES}} + \left(T_{\text{max}}^{\text{TES}} - T_{\text{min}}^{\text{TES}}\right) \frac{h_{\text{sat,liq}}^{\text{ORC}} - h_{\text{in}}^{\text{ORC}}}{h_{\text{out}}^{\text{ORC}} - h_{\text{in}}^{\text{ORC}}}\right) \leq 0 \tag{19}$$

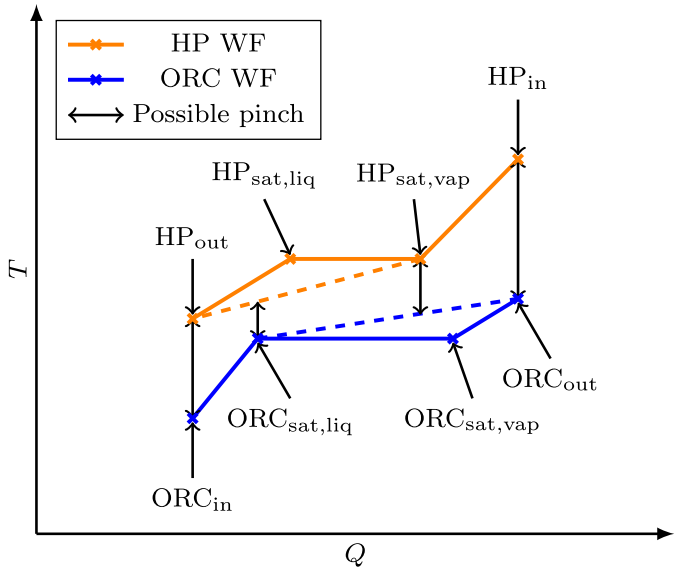

Fig. 5 T-Q-diagram of the TES for the RS modeling approach. All points where constraints ensure the minimum temperature difference are marked. For the shown example, y_{TES} is 0

$$T_{\text{sat}}^{\text{ORC}} + \Delta T_{\text{min}}^{\text{TES}} - \left(T_{\text{min}}^{\text{TES}} + \left(T_{\text{max}}^{\text{TES}} - T_{\text{min}}^{\text{TES}} \right) \frac{h_{\text{sat,vap}}^{\text{ORC}} - h_{\text{in}}^{\text{ORC}}}{h_{\text{out}}^{\text{ORC}} - h_{\text{in}}^{\text{ORC}}} \right) \leq 0 \tag{20}$$

$$T_{\text{out}}^{\text{ORC}} + \Delta T_{\text{min}}^{\text{TES}} - T_{\text{max}}^{\text{TES}} \leq 0 \tag{21}$$

Note that (15) and (20) are redundant as a constraint violation of these constraints is impossible without violating other constraints.

The second approach is a new approach that we call RS-approach, which is motivated by the RS modeling method. For an optimization of the RTE, the TES temperatures do not directly influence the objective. Instead, they are used to guarantee the minimum temperature difference between HP/TES and TES/ORC respectively. For given WF states, there can only be two outcomes: Either a set of feasible TES temperatures or not. Thus, we eliminate the TES temperatures from the model and instead add constraints that ensure the existence of feasible TES temperatures. When looking at the T-Q-diagram, existence of feasible TES temperatures is equivalent to linear separability of the HP and ORC states with an offset of $2\Delta T_{\text{min}}^{\text{TES}}$ ($\Delta T_{\text{min}}^{\text{TES}}$ between HP and TES plus $\Delta T_{\text{min}}^{\text{TES}}$ between TES and ORC).

First, we connect HP_{out} with $HP_{sat,vap}$, skipping $HP_{sat,liq}$, and $ORC_{sat,liq}$ with ORC_{out}, skipping $ORC_{sat,vap}$ (dashed lines in Fig. 5). In doing so, we make the shape of the HP curve concave and the shape of the ORC curve convex. To guarantee linear separability it is now sufficient to ensure the minimum temperature difference at every vertex of the new curves.

For the in- and outlet of the TES, this is straight-forward and results in the following constraints:

$$T_{\text{in}}^{\text{ORC}} + 2\Delta T_{\text{min}}^{\text{TES}} - T_{\text{out}}^{\text{HP}} \leq 0 \tag{22}$$

$$T_{\text{out}}^{\text{ORC}} + 2\Delta T_{\text{min}}^{\text{TES}} - T_{\text{in}}^{\text{HP}} \leq 0 \tag{23}$$

The first constraint can also be derived by combining (14) and (18) through the elimination of $T_{\text{min}}^{\text{TES}}$. For the second constraint, we would eliminate $T_{\text{max}}^{\text{TES}}$ from (17) and (21).

Next, we add constraints to ensure the minimum temperature difference at the two remaining vertices ($\text{HP}_{\text{sat,vap}}$ and $\text{ORC}_{\text{sat,liq}}$). Here, we need to consider two different cases based on the relative position of $\text{HP}_{\text{sat,vap}}$ and $\text{ORC}_{\text{sat,liq}}$ as this influences which opposing line we need to check the temperature difference against. For this, we introduce the binary variable y_{TES}. For $y_{\text{TES}} = 0$, $\text{ORC}_{\text{sat,liq}}$ is left of $\text{HP}_{\text{sat,vap}}$. For $y_{\text{TES}} = 1$, $\text{ORC}_{\text{sat,liq}}$ is right of $\text{HP}_{\text{sat,vap}}$. When $\text{ORC}_{\text{sat,liq}}$ and $\text{HP}_{\text{sat,vap}}$ share the same x-coordinate in the T-Q-diagram, y_{TES} can be either 0 or 1. We ensure this relationship by the following Big-M constraints:

$$\dot{m}^{\text{ORC}} \left(h_{\text{sat,liq}}^{\text{ORC}} - h_{\text{in}}^{\text{ORC}} \right) - \dot{m}^{\text{HP}} \left(h_{\text{sat,vap}}^{\text{HP}} - h_{\text{out}}^{\text{HP}} \right) \leq y_{\text{TES}} M \tag{24}$$

$$-\dot{m}^{\text{ORC}} \left(h_{\text{sat,liq}}^{\text{ORC}} - h_{\text{in}}^{\text{ORC}} \right) + \dot{m}^{\text{HP}} \left(h_{\text{sat,vap}}^{\text{HP}} - h_{\text{out}}^{\text{HP}} \right) \leq (1 - y_{\text{TES}})\, M \tag{25}$$

While Big-M constraints exhibit weak relaxations, they have little influence in our case. Our final CB model has only one binary variable (y_{TES}). MAiNGO branches first on the binary variables. Thus, after the first branching step the relaxations of the Big-M constraints are no longer considered. Therefore, the value of M has no influence on the computational performance. Another option would be to create two independent optimization problems that only consider $y_{\text{TES}} = 0$ or $y_{\text{TES}} = 1$, respectively (i.e., enumeration). These optimization problems are identical to those encountered after the first branching step of MAiNGO. Thus, enumeration for the TES model formulation was not further investigated. For the vertex $\text{HP}_{\text{sat,vap}}$, we add constraints ensuring the minimum temperature difference to the corresponding line of the ORC. These constraints are active/inactive based on the value of y_{TES}:

$$T_{\text{sat}}^{\text{ORC}} + \left(T_{\text{out}}^{\text{ORC}} - T_{\text{sat}}^{\text{ORC}} \right) \frac{\frac{\dot{m}^{\text{HP}}}{\dot{m}^{\text{ORC}}} h_{\text{sat,vap}}^{\text{HP}} - h_{\text{sat,liq}}^{\text{ORC}}}{h_{\text{out}}^{\text{ORC}} - h_{\text{sat,liq}}^{\text{ORC}}} - T_{\text{sat}}^{\text{HP}} + 2\Delta T_{\text{min}}^{\text{TES}} \leq y_{\text{TES}} M \tag{26}$$

$$T_{\text{in}}^{\text{ORC}} + \left(T_{\text{sat}}^{\text{ORC}} - T_{\text{in}}^{\text{ORC}} \right) \frac{\frac{\dot{m}^{\text{HP}}}{\dot{m}^{\text{ORC}}} h_{\text{sat,vap}}^{\text{HP}} - h_{\text{in}}^{\text{ORC}}}{h_{\text{sat,liq}}^{\text{ORC}} - h_{\text{in}}^{\text{ORC}}} - T_{\text{sat}}^{\text{HP}} + 2\Delta T_{\text{min}}^{\text{TES}} \leq (1 - y_{\text{TES}})\, M \tag{27}$$

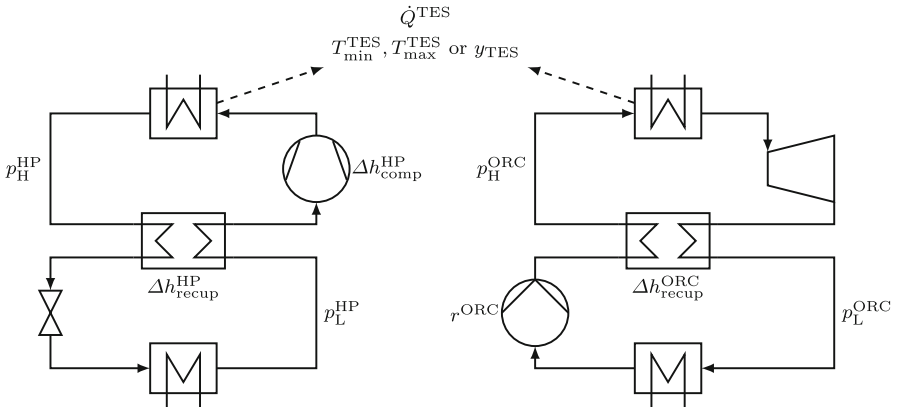

Fig. 6 Optimization variables of the CB model

For the vertex $\mathrm{ORC}_{\mathrm{sat,liq}}$, we add similar constraints:

$$T^{\mathrm{ORC}}_{\mathrm{sat}} - \left(T^{\mathrm{HP}}_{\mathrm{out}} + \left(T^{\mathrm{HP}}_{\mathrm{sat}} - T^{\mathrm{HP}}_{\mathrm{out}} \right) \frac{\frac{\dot{m}^{\mathrm{ORC}}}{\dot{m}^{\mathrm{HP}}} h^{\mathrm{ORC}}_{\mathrm{sat,liq}} - h^{\mathrm{HP}}_{\mathrm{out}}}{h^{\mathrm{HP}}_{\mathrm{sat,vap}} - h^{\mathrm{HP}}_{\mathrm{out}}} \right) + 2\Delta T^{\mathrm{TES}}_{\mathrm{min}} \leq y_{\mathrm{TES}} M \tag{28}$$

$$T^{\mathrm{ORC}}_{\mathrm{sat}} - \left(T^{\mathrm{HP}}_{\mathrm{sat}} + \left(T^{\mathrm{HP}}_{\mathrm{in}} - T^{\mathrm{HP}}_{\mathrm{sat}} \right) \frac{\frac{\dot{m}^{\mathrm{ORC}}}{\dot{m}^{\mathrm{HP}}} h^{\mathrm{ORC}}_{\mathrm{sat,liq}} - h^{\mathrm{HP}}_{\mathrm{sat,vap}}}{h^{\mathrm{HP}}_{\mathrm{in}} - h^{\mathrm{HP}}_{\mathrm{sat,vap}}} \right) + 2\Delta T^{\mathrm{TES}}_{\mathrm{min}} \leq (1 - y_{\mathrm{TES}})\, M \tag{29}$$

In doing so, we have replaced two continuous variables with a single binary variable with the RS-approach.

4.5 Process optimization

Bongartz and Mitsos (2017) show that for global optimization of flowsheets, reducing the number of optimization variables up to the number of degrees of freedom (i.e., following the RS modeling approach) is frequently computationally superior to a full-space modeling approach where all model variables are optimization variables. However, keeping a limited number of intermediate variables as optimization variables is potentially beneficial (Najman et al. 2021). Therefore, we aim to set up a model with a low number of optimization variables that exhibits a high computational performance.

As we do not consider sizing and capital cost of the CB, the absolute values of the mass flows are not of interest. Thus, we use only the ratio between the mass flow in ORC and HP $r^{\mathrm{ORC}} = \dot{m}^{\mathrm{ORC}}/\dot{m}^{\mathrm{HP}}$ as an optimization variable. Further, the pressure levels of both processes ($p^{\mathrm{HP}}_{\mathrm{L}}$, $p^{\mathrm{HP}}_{\mathrm{H}}$, $p^{\mathrm{ORC}}_{\mathrm{L}}$, and $p^{\mathrm{ORC}}_{\mathrm{H}}$), the thermal energy transferred/released to/from the TES ($\dot{Q}^{\mathrm{TES}}$), and the enthalpy increase/decrease in the recuperators ($\Delta h^{\mathrm{HP}}_{\mathrm{recup}}$ and $\Delta h^{\mathrm{ORC}}_{\mathrm{recup}}$) are optimization variables. We add more optimiza-

Table 2 Description of optimization variables used in the CB model

Optimization variable	Description
$p_{\mathrm{L}}^{\mathrm{HP}}$	Low pressure level of HP
$p_{\mathrm{H}}^{\mathrm{HP}}$	High pressure level of HP
$p_{\mathrm{L}}^{\mathrm{ORC}}$	Low pressure level of ORC
$p_{\mathrm{H}}^{\mathrm{ORC}}$	High pressure level of ORC
r^{ORC}	Ratio of mass flows in ORC and HP
$\dot{Q}^{\mathrm{TES}}$	Heat flow to/from TES
$\Delta h_{\mathrm{recup}}^{\mathrm{HP}}$	Enthalpy increase in HP recuperator
$\Delta h_{\mathrm{recup}}^{\mathrm{ORC}}$	Enthalpy increase in ORC recuperator
$\Delta h_{\mathrm{comp}}^{\mathrm{HP}}$	Enthalpy increase in HP compressor
T-approach:	
$T_{\mathrm{min}}^{\mathrm{TES}}$	Minimum temperature of TES medium
$T_{\mathrm{max}}^{\mathrm{TES}}$	Maximum temperature of TES medium
RS-approach:	
y_{TES}	Binary variable for TES temperature profiles

tion variables depending on the modeling approach for the TES. For the T-approach, we add the minimum and maximum storage medium temperatures as optimization variables ($T_{\mathrm{min}}^{\mathrm{TES}}$ and $T_{\mathrm{max}}^{\mathrm{TES}}$). For the RS-approach, we add the binary variable y_{TES}. Motivated by the work of Najman et al. (2021), we look for intermediate variables that improve computational performance by reintroduction as optimization variables. For this, we investigate the enthalpy differences of HP compressor, ORC turbine, and ORC pump as they directly influence the objective function. We find that only the HP compressor enthalpy difference improves computational performance. Thus, we add it together with a matching equality constraint. Overall, we obtain 9 or 10 optimization variables depending on the TES model formulation. A summary is given in Fig. 6 and Table 2. The variable bounds are listed in the appendix (A.1).

While the WF selection could be directly integrated into the optimization model, we apply enumeration. Although this leads to a large number of problems that need to be solved (one for each possible WF combination), the resulting problems are much smaller. Also, this approach provides an optimal CB design and RTE for every WF combination.

Following the approach of Huster et al. (2020a), we add relaxation-specific constraints to the problem formulation to tighten relaxations. The relaxation-specific constraints ensure increasing/decreasing temperatures and enthalpies in rotating equipment and heat exchangers.

Table 3 Isentropic efficiencies of rotating equipment used in the case study

	η_{is}	Source
Compressor	85 %	Liang et al. (2022)
Pump	85 %	Tillmanns et al. (2022)
Turbine	90 %	Tillmanns et al. (2022)

5 Implementation

We implement the proposed framework in Python. We use the thermodynamic library CoolProp (Bell et al. 2014, 2023) for all thermodynamic data. We train all ANNs using Tensorflow (Abadi et al. 2016). As Tensorflow does not natively support the LM training algorithm, we use the open-source implementation by Di Marco (2020). We split up the training data for the ANNs with two-dimensional input into minibatches of $\sim$ 1000 data points. For the custom training loop, it is required to evaluate the ANN relaxations. For this, we use a utility function available in the MAiNGO repository. We parallelize the training process using a straightforward parallelization method. This approach distributes the WFs are distributed across the available cores. Each core is responsible for training all ANNs associated with its designated WF. We implement the hybrid CB model and both TES model formulations utilizing the Python interface to MAiNGO (maingopy v0.7.2). Using the MeLOn toolbox (melonpy v0.0.10), we integrate the ANNs into the model formulation. We run the optimizations on 20 cores of a CLAIX-2023 node of the high performance cluster (HPC) of RWTH Aachen University using the parallel implementation of MAiNGO. During pre-processing, we perform 25 local searches. Also, we adjust the optimality tolerance to an absolute value of 0.001. This is equivalent to a final gap of 0.1 % in the RTE. For the remaining settings, we use the MAiNGO default values.

6 Results

6.1 Case study

As RTE increases with decreasing cold storage temperature, we assume a moderate ambient temperature of $T_{env} = 15\,°C$. We set the minimum temperature difference in the TES, the recuperator, and the ambient heat exchangers to 5 K. CBs are heavily dependent on the isentropic efficiencies of the rotating equipment. Table 3 shows the efficiencies we use for our case study. We select values that were also used by Tillmanns et al. (2022). However, we decrease the compressor efficiency from 88 % to 85 % as the original value lies outside of the range for compressor efficiencies reported in Liang et al. (2022). The other efficiencies are within the reported intervals.

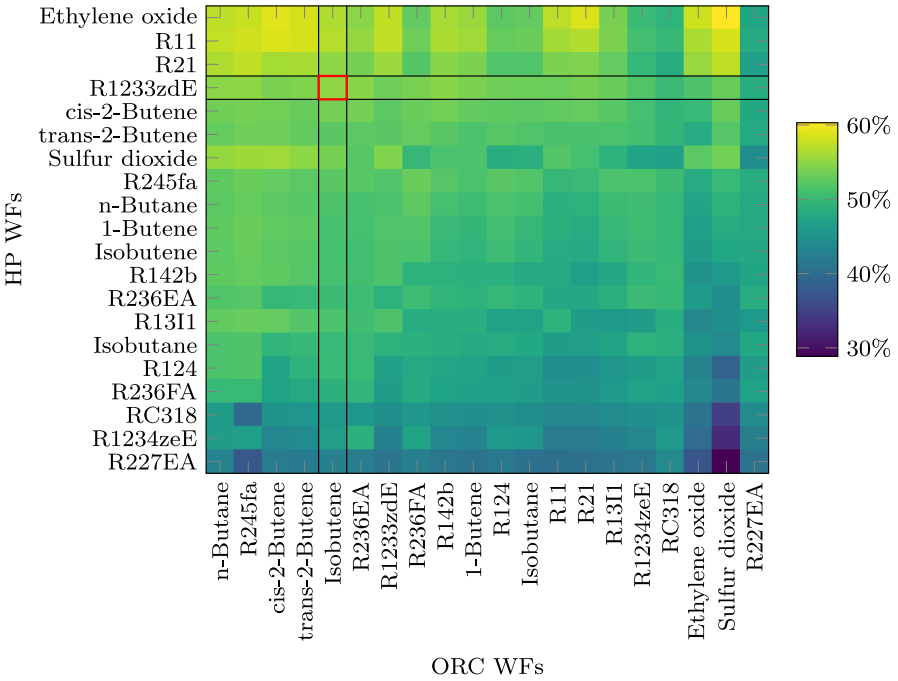

Fig. 7 Heatmap of maximum RTEs for all WF combinations. The combination R1233zd(E) / Isobutene (investigated in Sections **??**, 6.4, and A.2) is highlighted

Table 4 Top 5 and Bottom 5 WF combinations according to their RTE

HP WF	ORC WF	ϵ
Ethylene oxide	Sulfur dioxide	60.3 %
Ethylene oxide	cis-2-Butene	59.0 %
R11	cis-2-Butene	58.6 %
Ethylene oxide	R21	58.6 %
R11	Sulfur dioxide	58.4 %
R227EA	R245fa	37.4 %
R227EA	Ethylene oxide	37.2 %
RC318	Sulfur dioxide	34.7 %
R1234ze(E)	Sulfur dioxide	32.5 %
R227EA	Sulfur dioxide	28.8 %

6.2 WF screening

CoolProp provides thermodynamic data for a total of 123 fluids. The WF preselection results in 20 WF candidates which we consider for the screening. Thus, we optimize the CB for 400 different WF combinations. The results of the WF screening are presented as a heatmap in Fig. 7. Overall, we observe efficiencies in the range 30 % to 60 %.

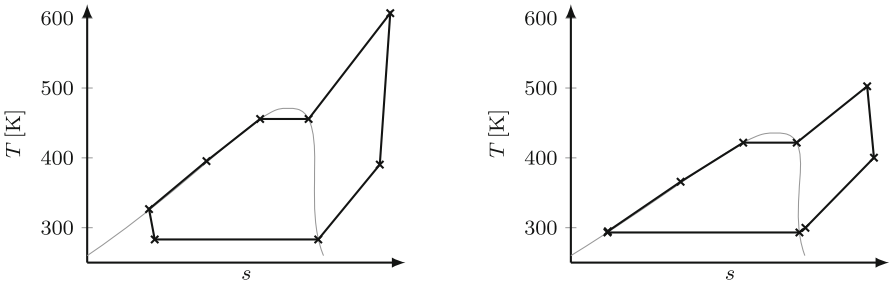

(a) Optimal HP (R11) (b) Optimal ORC (cis-2-Butene)

Fig. 8 T-s-diagrams of the optimized CB using R11 as HP WF and cis-2-Butene as ORC WF

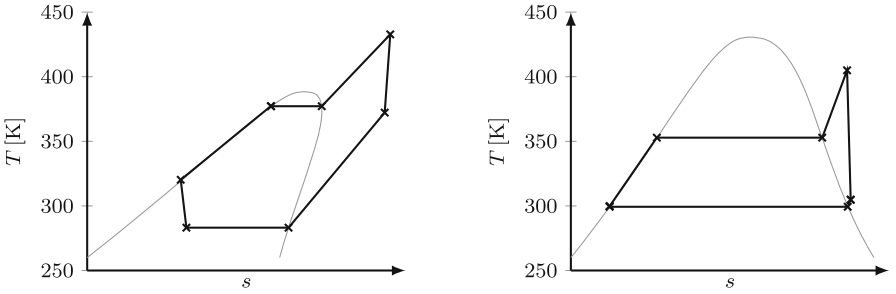

(a) Optimal HP (RC318) (b) Optimal ORC (sulfur dioxide)

Fig. 9 T-s-diagrams of the optimized CB using RC318 as HP WF and sulfur dioxide as ORC WF

In the heatmap, it can be seen that the HP WF has a larger influence on the RTE than the ORC WF. For example, ethylene oxide, R11, and R21 generally lead to high RTEs when used as HP WF. For the ORC WFs, such a trend can only be observed for R227EA and RC318, which lead to generally low RTEs. In Table 4 the 5 best and 5 worst WF combinations are given. Sulfur dioxide appears multiple times as an ORC WF in both lists, again highlighting the larger influence of the HP WF on RTE. We further investigate this topic by plotting the T-s-diagrams of a member of the top 5 and bottom 5 WF combination in Fig. 8 and Fig. 9 respectively. For R11 / cis-2-Butene (Fig. 8, $\epsilon = 58.6\,\%$) we see that HP and ORC operate close to their critical pressure. Also, the critical temperature of the HP WF is around 35 K higher than the critical temperature of the ORC WF. Both processes exhibit only a small evaporation enthalpy at the high pressure level. This allows for a close match of the temperature profiles in the TES. Also, large amounts of heat are recovered in the recuperator during charging and discharging. For RC318 / sulfur dioxide (Fig. 9, $\epsilon = 34.7\,\%$) the processes look very different. Overall, the CB operates at lower temperature levels, constrained by the low critical temperature of RC318. These lower temperatures prevent the ORC from operating close to the critical pressure as the ORC WF has a larger critical temperature than the HP WF (~ 42 K). Thus, the ORC has to overcome a large evaporation enthalpy at the high pressure level, leading to a mismatch of temperature profiles in the TES.

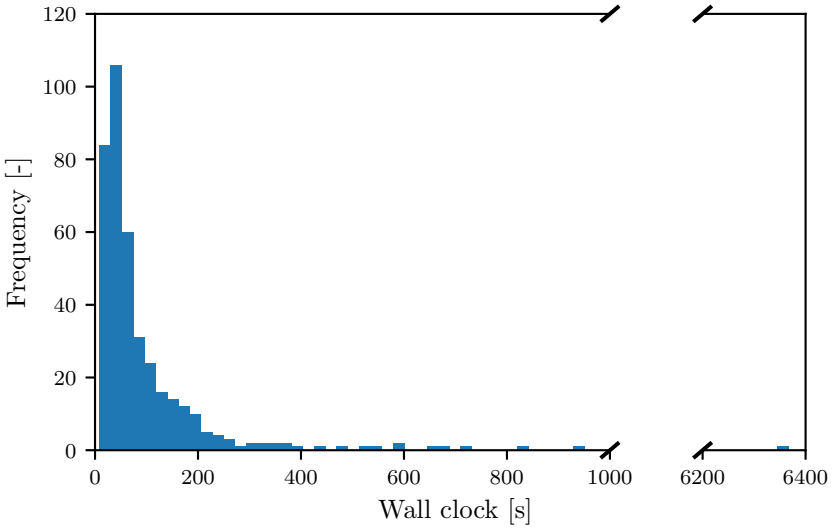

Fig. 10 Histogram of wall-clock times of optimization runs

Besides performance, several other criteria are relevant for the WF selection (e.g., safety, toxicity, ozone depletion potential (ODP), global warming potential (GWP)). Arpagaus et al. (2018) summarize these characteristics for most of the considered WFs. The top WFs that we identified in this study do either exhibit high ODP or GWP or are unsafe. The best safe WF combination with low ODP and GWP is R1233zd(E) for the HP and Isobutene for the ORC with an RTE $\epsilon = 55.1\,\%$. Thus, we focus on this WF pairing for Sections **??** and 6.4.

Figure 10 shows a histogram of the wall-clock times for all 400 optimization runs. The vast majority of runs converge to global optimality in less than 200 s (89 %). However, there are outliers up to a wall-clock time of almost 2 h. In total, the WF screening took 17.61 h.

To determine the necessity of DGO, we investigate the difference between solutions found by local searches and the global solution. Most optimization runs find the global solution during the initial multistart. However, out of 400 WF combinations, 37 improve the RTE by an absolute value of at least 1 %. For 6 WF combinations, the multistart does not result in any feasible solutions at all. In Fig. 11, we present the evolution of local solutions during the B&B for the 20 WF combinations with the largest gap between initial solution and global solution. It can be seen that only considering local optimization for the screening leads to overlooking promising WF candidates which would be found via DGO. Processes that are infeasible according to the local solver can, in reality, exhibit high RTEs.

6.3 Influence of proposed ANN training procedure

We compare the proposed multi-candidate ANN training procedure (cf. Sect. 4.3) to a conventional approach, where a single ANN candidate is trained and selected

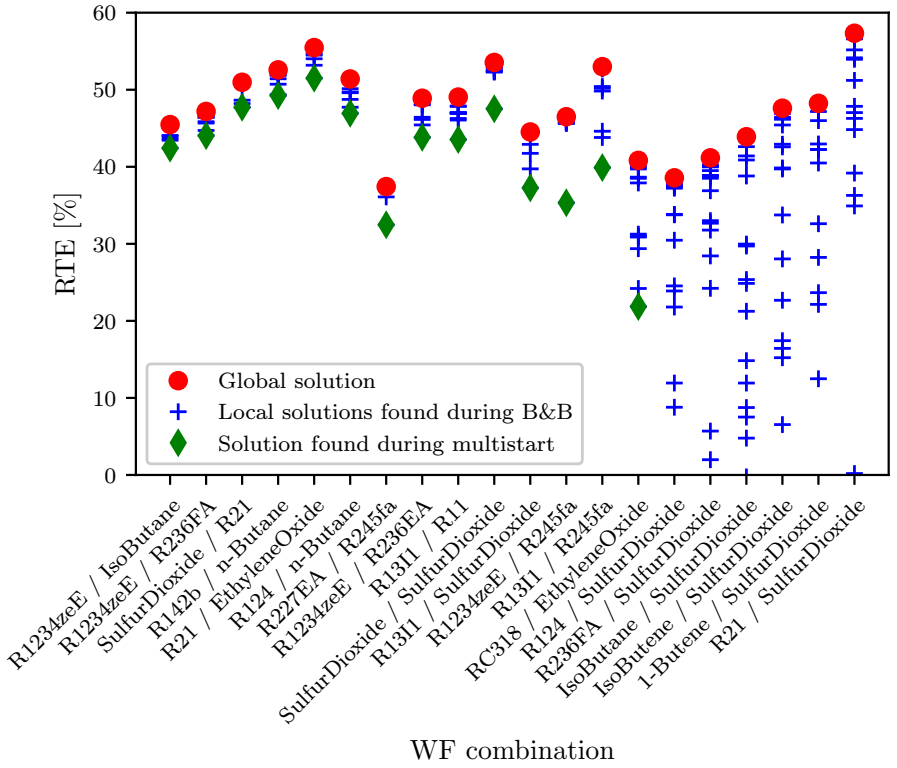

Fig. 11 This figure compares the best local solution found during the initial multistart with the global solution. We present the 20 WF combinations with the largest gap between those solutions. Also, local solutions found during branch-and-bound (B&B) are shown. For the six rightmost WF combinations, no feasible solution is found during multistart

based solely on its MSE. The conventional approach is equivalent to the proposed approach when only one ANN candidate is trained ($k = 1$). To account for the randomness in ANN training, we perform multiple runs of the conventional approach using different random seeds for the ANN training. We compare the approaches for the WF combination R1233zd(E) / Isobutene. Each run results in a single set of all ANNs required for the CB model. For every set of trained ANNs, we solve the CB model to global optimality. As we are testing entire sets of ANNs, the effect of ANNs with tight relaxations might be counteracted by ANNs with loose relaxations in the same set. However, this testing gives a realistic estimate of the expected performance improvement of the proposed method.

Table 5 shows the wall-clock times for the proposed procedure, and 5 runs with the conventional approach. Two runs (# 1 and # 4) converge slightly slower than the proposed method. Another two runs (# 3 and # 5) are between 3 and 6 times slower. Run # 2, however, does not reach convergence after 1 h with a large remaining relative gap. Overall, the proposed procedure can lead to a large improvement in computational performance. Also, we observe a large variation in wall-clock times

Table 5 Influence of proposed ANN training procedure with $k = 5$. The WF combination R1233zd(E) / Isobutene is used for demonstration. In the second run (*) of the conventional approach, a time-out occurred after 1 h. At that time, the remaining relative optimality gap of the DGO was 162 %

Method	Conventional Approach (5 Runs)					Proposed Approach
	# 1	# 2	# 3	# 4	# 5	
Wall-clock Time	106 s	1 h*	273.98 s	95.5 s	572.3 s	94.5 s

Table 6 Comparison of optimization runs using the two different TES modeling approaches for the WF combination R1233zd(E) / Isobutene

	RS-approach	T-approach
Wall-clock time [s]	94.48	5327.11
Iterations [-]	4.15×10^5	2.54×10^6
ϵ [%]	55.07	55.07

with the conventional approach. It appears that the ANN training can sometimes (depending on the random initialization) result in a set of ANNs that make the final CB model much more challenging to optimize. Due to the extreme outlier (run # 2), we assume that some ANNs of the set have a larger influence on the wall-clock time than others. If all ANNs had a similar influence, we would expect a tighter distribution of wall-clock times as the influence of a single outlier ANN would be smoothed out by the other ANNs.

6.4 Influence of TES model formulation

We compare both TES modeling approaches in Table 6. A T-Q-diagram of the TES for both approaches is shown in Fig. 12. We see that both approaches result in exactly the same global optimum. However, the RS-approach requires a wall-clock time that is smaller by a factor of $\sim$ 56. For both approaches, the global optimum is found during the initial multistart. Besides the computational advantage, the RS-approach does not require bounds on the maximum/minimum TES temperature. In a small subsequent optimization problem, the TES temperatures can be determined based on the optimal point given by the RS-approach. However, during the optimization of the CB, information about the TES temperatures is no longer directly available. Thus, the RS-approach can only be used to optimize for efficiency. Optimizing the TES sizing requires information such as the storage size and pressure, which are functions of storage temperatures and storage medium. This information is unavailable during the optimization with the RS-approach.

7 Conclusion

We used DGO to screen WF combinations for ORC-based CBs with a single high-temperature TES, considering accurate fluid properties. Even this simple CB layout allows for RTEs of up to 60 %. When limiting the WF selection to non-toxic, low

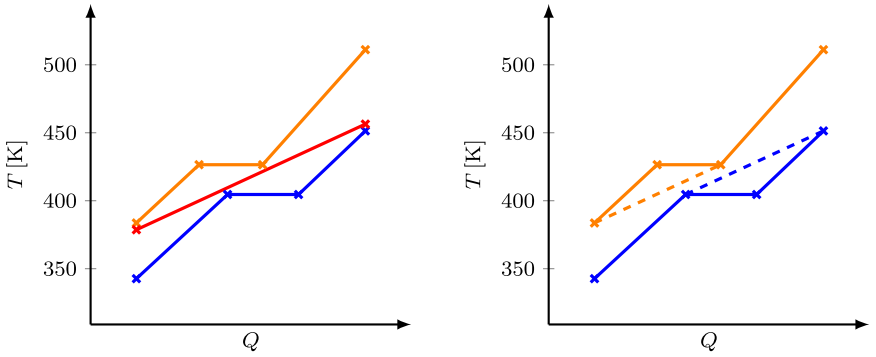

(a) T-approach (b) RS-approach

Fig. 12 T-Q-diagram of global optimum for both TES modeling approaches. The CB uses the WF combination R1233zd(E) / Isobutene

ODP, and low GWP WFs, RTEs of up to 55 % are possible. To make the DGO of all 400 WF combinations computationally tractable, we had to make the following improvements to the model formulation. We proposed a RS modeling approach for the TES that enables significant savings in computational time by replacing two continuous optimization variables by a single binary variable. However, it can only be applied when storage sizing is not included in the model, as information regarding the TES is no longer explicitly available during optimization. We observed that McCormick relaxations of ANNs of similar size and accuracy can vary strongly and have a large influence on computational performance. Thus, we proposed a new ANN training procedure that considers the McCormick relaxations and reduces worst-case wall-clock times compared to a conventional approach. This allowed us to solve all 400 optimization problems to global optimality in less than 24 h, demonstrating that DGO can be used for such high-level screening tasks if one uses a tailored model. Further, we demonstrated that without DGO promising WF candidates are overlooked as the local solver fails in identifying the global optimum.

Alternative process variants that minimize exergy losses can achieve further RTE improvements. As we already take optimistic assumptions for the efficiency of the rotating equipment, minimizing the exergy loss of heat transfer to and from the TES is one of the most promising options. For this, a better match of WF and TES temperature profile is required. Options to modify the WF temperature profile include transcritical operation or the use of WF mixtures. Previous work of our group has investigated both of these options for ORCs (Huster et al. 2020b, c). The TES temperature profile can be modified by allowing for multiple storage tanks (e.g., Steinmann 2014). Also, the CB investigation can be broadened by considering the use of waste heat as the HP heat source, the use of a designated cold storage instead of the environment, or the direct use of thermal energy stored in the TES. Modeling these CB variants can be done with only minor modifications to the presented work. Expanding the model by incorporating cost correlations is of high interest for future work. This would enable DGO of CB design via an economic objective function. The most promising WF com-

binations identified in this work should be subjected to such an investigation. Further, consideration of off-design operation should be included in the process optimization. Dumont et al. (2020) identify off-design operation as one of the main challenges in CB development. For ORCs, Langiu et al. (2022) consider multiple ambient temperatures for the simultaneous optimization of design and operation of an air-cooled ORC. This work can be extended to the considered CB. The reason for the sometimes loose ANN relaxations and ways to prevent it (besides our proposed method) need to be further investigated. While the proposed TES model formulation is very specific to the CB, it might be applicable to other application within energy engineering. E.g., one could imagine a process, in which a heat transfer fluid (HTF) is utilized to transfer heat between an evaporator and a condenser. Generalizing the RS TES model formulation to other WF and TES temperature profiles besides the ones used in this work, could also improve the computational tractability of the DGO of more complex CB layouts.

A Appendix

A.1 Optimization variable bounds

For the CB model, we use WF dependent optimization variable bounds. We take the values used in Huster et al. (2019b) for the bounds on the pressure levels. For the ratio of mass flows r^{ORC}, we first calculate the ratio between average evaporation enthalpy of HP and ORC WF as a reference value. The lower and upper bound of r^{ORC} we set to $2/3$ and $3/2$ of this reference respectively. These factors give a good trade-off between computational performance and the size of the search space.

$$
\begin{aligned}
p_{\mathrm{L}}^{\mathrm{HP}} &\in [0.2\,\mathrm{bar}, 10\,\mathrm{bar}] \\
p_{\mathrm{H}}^{\mathrm{HP}} &\in \left[0.5\,\mathrm{bar}, 0.8 * p_{\mathrm{crit}}^{\mathrm{HP}}\right] \\
p_{\mathrm{L}}^{\mathrm{ORC}} &\in [0.2\,\mathrm{bar}, 10\,\mathrm{bar}] \\
p_{\mathrm{H}}^{\mathrm{ORC}} &\in \left[0.5\,\mathrm{bar}, 0.8 * p_{\mathrm{crit}}^{\mathrm{ORC}}\right] \\
r^{\mathrm{ORC}} = \frac{\dot{m}^{\mathrm{ORC}}}{\dot{m}^{\mathrm{HP}}} &\in \left[\frac{2}{3}\frac{\Delta h_{\mathrm{evap,avg}}^{\mathrm{HP}}}{\Delta h_{\mathrm{evap,avg}}^{\mathrm{ORC}}}, \frac{3}{2}\frac{\Delta h_{\mathrm{evap,avg}}^{\mathrm{HP}}}{\Delta h_{\mathrm{evap,avg}}^{\mathrm{ORC}}}\right] \\
\dot{Q}^{\mathrm{TES}} &\in \Big[\dot{m}^{\mathrm{HP}} \Delta h_{\mathrm{evap}}^{\mathrm{HP}}\left(p_{\mathrm{max}}^{\mathrm{HP}}\right), \\
&\qquad \dot{m}^{\mathrm{HP}}\left(h_{\mathrm{vap}}^{\mathrm{HP}}\left(p_{\mathrm{max}}^{\mathrm{HP}}, T_{\mathrm{max}}\right) - h_{\mathrm{liq}}^{\mathrm{HP}}\left(p_{\mathrm{max}}^{\mathrm{HP}}, T_{\mathrm{amb}}\right)\right)\Big] \\
\Delta h_{\mathrm{recup}}^{\mathrm{HP}} &\in \left[0, h_{\mathrm{sat,liq}}^{\mathrm{HP}}(p_{\mathrm{max}}^{\mathrm{HP}}) - h_{\mathrm{liq}}^{\mathrm{HP}}(p_{\mathrm{max}}^{\mathrm{HP}}, T_{\mathrm{amb}})\right] \\
\Delta h_{\mathrm{recup}}^{\mathrm{ORC}} &\in \left[0, h_{\mathrm{sat,liq}}^{\mathrm{ORC}}(p_{\mathrm{max}}^{\mathrm{ORC}}) - h_{\mathrm{liq}}^{\mathrm{ORC}}(p_{\mathrm{max}}^{\mathrm{ORC}}, T_{\mathrm{amb}})\right] \\
\Delta h_{\mathrm{comp}}^{\mathrm{HP}} &\in \left[0, h_{\mathrm{vap}}^{\mathrm{HP}}(p_{\mathrm{max}}^{\mathrm{HP}}, s_{\mathrm{sat,vap}}^{\mathrm{HP}}(p_{\mathrm{min}})) - h_{\mathrm{sat,vap}}^{\mathrm{HP}}(p_{\mathrm{min}}^{\mathrm{HP}})\right]
\end{aligned}
$$

T-approach:

Table 7 Influence of adding compressor enthalpy difference as additional optimization variable for the WF combination R1233zd(E) / Isobutene. The optimization run without the additional optimization variable (*) terminated after 1 h with a remaining relative gap of 22.7 %

	Wall-clock time	# Iterations
RS-Comp	94.5 s	415167
RS-Base	1 h*	1 560 000

$$T_{\text{min}}^{\text{TES}} \in [320\,\text{K}, 450\,\text{K}]$$
$$T_{\text{max}}^{\text{TES}} \in [350\,\text{K}, 520\,\text{K}]$$

RS-approach:

$$y_{\text{TES}} \in \{0, 1\}$$

A.2 Influence of HP compressor optimization variable

As described in Sect. 4.5, we add the HP compressor enthalpy difference as an additional optimization variable. Here, we investigate the influence of this variable on the computational performance. Both model formulations result in the same solution point. However, they differ in the wall-clock time as shown in Table 7. Without the additional optimization variable (RS-Base), the optimization terminates after the maximum time of 1 h. As a drawback, adding it requires setting valid bounds on the new optimization variable.

Acknowledgements The authors gratefully acknowledge the financial support of the Kopernikus project SynErgie by the Federal Ministry of Education and Research (BMBF) and the project supervision by the project management organization Projektträger Jülich (PtJ). Computations were performed with computing resources granted by RWTH Aachen University.

Author Contributions The basic idea of the TES modeling approach was developed by Jannik Lüthje. Alexander Mitsos helped in refining it. The idea for the modification to the ANN training procedure was developed by Jannik Lüthje with the support of Marco Langiu. Jannik Lüthje and Marco Langiu performed the literature review. The hybrid CB model, case study, and formulation of the optimization problem were developed and implemented by Jannik Lüthje. Jannik Lüthje performed the optimization runs, analyzed the results, and wrote the first draft of the manuscript. Alexander Mitsos and Marco Langiu commented on the manuscript. Alexander Mitsos supervised the work.

Funding Open Access funding enabled and organized by Projekt DEAL. This work has received funding by the Kopernikus project SynErgie by the Federal Ministry of Education and Research (BMBF).

Data Availability Data for the ANN training was generated with CoolProp. The trained ANNs, the model formulation, and the optimization results are publicly available at http://permalink.avt.rwth-aachen.de/?id=305911.

Declarations

Ethics approval and consent to participate Not applicable.

Consent for publication Not applicable.

Competing interests The authors declare no competing interests.

Open Access This article is licensed under a Creative Commons Attribution 4.0 International License, which permits use, sharing, adaptation, distribution and reproduction in any medium or format, as long as you give appropriate credit to the original author(s) and the source, provide a link to the Creative Commons licence, and indicate if changes were made. The images or other third party material in this article are included in the article's Creative Commons licence, unless indicated otherwise in a credit line to the material. If material is not included in the article's Creative Commons licence and your intended use is not permitted by statutory regulation or exceeds the permitted use, you will need to obtain permission directly from the copyright holder. To view a copy of this licence, visit http://creativecommons.org/licenses/by/4.0/.

References

Abadi M, Agarwal A, Barham P, Brevdo E, Chen Z, Citro C, Corrado GS, Davis A, Dean J, Devin M, Ghemawat S, Goodfellow I, Harp A, Irving G, Isard M, Jia Y, Jozefowicz R, Kaiser L, Kudlur M, Levenberg J, Mane D, Monga R, Moore S, Murray D, Olah C, Schuster M, Shlens J, Steiner B, Sutskever I, Talwar K, Tucker P, Vanhoucke V, Vasudevan V, Viegas F, Vinyals O, Warden P, Wattenberg M, Wicke M, Yu Y, Zheng X (2016) TensorFlow: Large-Scale Machine Learning on Heterogeneous Distributed Systems. arxiv:org/pdf/1603.04467

Arpagaus C, Bless F, Uhlmann M, Schiffmann J, Bertsch SS (2018) High temperature heat pumps: Market overview, state of the art, research status, refrigerants, and application potentials. Energy 152:985–1010. https://doi.org/10.1016/j.energy.2018.03.166https://www.sciencedirect.com/science/article/pii/S0360544218305759

Asprion N, Böttcher R, Pack R, Stavrou ME, Höller J, Schwientek J, Bortz M (2019) Gray-Box Modeling for the Optimization of Chemical Processes. Chem-Ing-Tech 91(3):305–313. https://doi.org/10.1002/cite.201800086https://onlinelibrary.wiley.com/doi/10.1002/cite.201800086

Bao J, Zhao L (2013) A review of working fluid and expander selections for organic Rankine cycle. Renew Sustain Energy Rev 24:325–342. https://doi.org/10.1016/j.rser.2013.03.040https://www.sciencedirect.com/science/article/pii/S1364032113001998

Bell IH, Wronski J, Quoilin S, Lemort V (2014) Pure and Pseudo-pure Fluid Thermophysical Property Evaluation and the Open-Source Thermophysical Property Library CoolProp. Ind Eng Chem Res 53(6):2498–2508. https://doi.org/10.1021/ie4033999

Bell IH, Wronski J, Quoilin S, Lemort V (2023) CoolProp 6.6.0 documentation. http://www.coolprop.org/

Benato A, Stoppato A (2018) Heat transfer fluid and material selection for an innovative Pumped Thermal Electricity Storage system. Energy 147:155–168. https://doi.org/10.1016/j.energy.2018.01.045

Bongartz D, Mitsos A (2017) Deterministic global optimization of process flowsheets in a reduced space using McCormick relaxations. J Global Optim 69(4):761–796. https://doi.org/10.1007/s10898-017-0547-4

Bongartz D, Najman J, Sass S, Mitsos A (2018) MAiNGO: McCormick based Algorithm for mixed integer Nonlinear Global Optimization. Tech. rep., Process Systems Engineering (AVT. SVT), RWTH Aachen University, available at https://www.avt.rwth-aachen.de/global/show_document.asp?id=aaaaaaaaabclahw, accessed 10 November 2021

Bradley W, Kim J, Kilwein Z, Blakely L, Eydenberg M, Jalvin J, Laird C, Boukouvala F (2022) Perspectives on the integration between first-principles and data-driven modeling. Comput Chem Eng 166:107898. https://doi.org/10.1016/j.compchemeng.2022.107898https://www.sciencedirect.com/science/article/pii/S0098135422002368

Cebulla F, Haas J, Eichman J, Nowak W, Mancarella P (2018) How much electrical energy storage do we need? A synthesis for the U.S., Europe, and Germany. J Clean Prod 181:449–459. https://doi.org/10.1016/j.jclepro.2018.01.144https://www.sciencedirect.com/science/article/pii/S0959652618301665

Ceccon F, Jalving J, Haddad J, Thebelt A, Tsay C, Laird CD, Misener R (2022) OMLT: Optimization & Machine Learning Toolkit. J Mach Learn Res 23(349):1–8

Desrues T, Ruer J, Marty P, Fourmigué JF (2010) A thermal energy storage process for large scale electric applications. Appl Therm Eng 30(5):425–432. https://doi.org/10.1016/j.applthermaleng.2009.10.002

Di Marco F (2020) Tensorflow implementation of Levenberg-Marquardt training algorithm. https://github.com/fabiodimarco/tf-levenberg-marquardt

Dumont O, Frate GF, Pillai A, Lecompte S, De Paepe M, Lemort V (2020) Carnot battery technology: A state-of-the-art review. J Energy Storage 32:101756. https://doi.org/10.1016/j.est.2020.101756

Durth M, Prieto C, Rodríguez-Sánchez A, Patiño-Rodríguez D, Cabeza LF (2019) Effects of sodium nitrate concentration on thermophysical properties of solar salts and on the thermal energy storage cost. Sol Energy 182:57–63. https://doi.org/10.1016/j.solener.2019.02.038https://www.sciencedirect.com/science/article/pii/S0038092X19301641

Eppinger B, Zigan L, Karl J, Will S (2020) Pumped thermal energy storage with heat pump-ORC-systems: Comparison of latent and sensible thermal storages for various fluids. Appl Energy 280:115940. https://doi.org/10.1016/j.apenergy.2020.115940https://www.sciencedirect.com/science/article/pii/S0306261920313970

Fan R, Xi H (2022) Energy, exergy, economic (3E) analysis, optimization and comparison of different Carnot battery systems for energy storage. Energ Convers Manage 252:115037. https://doi.org/10.1016/j.enconman.2021.115037

Frate GF, Ferrari L, Desideri U (2020) Multi-criteria investigation of a pumped thermal electricity storage (PTES) system with thermal integration and sensible heat storage. Energ Convers Manage 208:112530. https://doi.org/10.1016/j.enconman.2020.112530https://www.sciencedirect.com/science/article/pii/S1364032113001998

Hagan MT, Menhaj MB (1994) Training feedforward networks with the Marquardt algorithm. IEEE Trans Neural Networks 5(6):989–993. https://doi.org/10.1109/72.329697

Hassan AH, O'Donoghue L, Sánchez-Canales V, Corberán JM, Payá J, Jockenhöfer H (2020) Thermodynamic analysis of high-temperature pumped thermal energy storage systems: Refrigerant selection, performance and limitations. Energy Rep 6:147–159. https://doi.org/10.1016/j.egyr.2020.05.010

Huster WR, Schweidtmann AM, Mitsos A (2019) Impact of Accurate Working Fluid Properties on the Globally Optimal Design of an Organic Rankine Cycle. Comput Aided Chem Eng 47:427–432. https://doi.org/10.1016/b978-0-12-818597-1.50068-0

Huster WR, Schweidtmann AM, Mitsos A (2019) Working Fluid Selection for Organic Rankine Cycles Via Deterministic Global Optimization of Design and Operation. Optim Eng 21(2):517–536. https://doi.org/10.1007/s11081-019-09454-1

Huster WR, Schweidtmann AM, Lüthje JT, Mitsos A (2020a) Deterministic global superstructure-based optimization of an organic rankine cycle. Comput Chem Eng 141:106996. https://doi.org/10.1016/j.compchemeng.2020.106996

Huster WR, Schweidtmann AM, Mitsos A (2020b) Globally optimal working fluid mixture composition for geothermal power cycles. Energy 212:118731. https://doi.org/10.1016/j.energy.2020.118731

Huster WR, Schweidtmann AM, Mitsos A (2020c) Hybrid Mechanistic Data-Driven Modeling for the Deterministic Global Optimization of a Transcritical Organic Rankine Cycle. In: Comput. Aided Chem. Eng., vol 48, Elsevier, pp 1765–1770, https://doi.org/10.1016/b978-0-12-823377-1.50295-0

Huster WR, Schweidtmann AM, Mitsos A (2020d) Working fluid selection for organic rankine cycles via deterministic global optimization of design and operation. Optim Eng 21(2):517–536. https://doi.org/10.1007/s11081-019-09454-1https://link.springer.com/article/10.1007/s11081-019-09454-1

Jockenhöfer H, Steinmann WD, Bauer D (2018) Detailed numerical investigation of a pumped thermal energy storage with low temperature heat integration. Energy 145:665–676. https://doi.org/10.1016/j.energy.2017.12.087

Kahrs O, Marquardt W (2007) The validity domain of hybrid models and its application in process optimization. Chem Eng Process Process Intensif 46(11):1054–1066. https://doi.org/10.1016/j.cep.2007.02.031https://www.sciencedirect.com/science/article/pii/S0255270107001134

Koen A, Farres-Antunez P, Macnaghten J, White A (2021) A low-temperature glide cycle for pumped thermal energy storage. J Energy Storage 42:103038. https://doi.org/10.1016/j.est.2021.103038https://www.sciencedirect.com/science/article/pii/S2352152X21007453

Langiu M, Dahmen M, Mitsos A (2022) Simultaneous optimization of design and operation of an air-cooled geothermal ORC under consideration of multiple operating points. Comput Chem Eng 161:107745. https://doi.org/10.1016/j.compchemeng.2022.107745

Laughlin RB (2017) Pumped thermal grid storage with heat exchange. J Renewable Sustainable Energy 9(4):044103. https://doi.org/10.1063/1.4994054

Lemmon EW, Bell IH, Huber ML, McLinden MO (2018) NIST Standard Reference Database 23: Reference Fluid Thermodynamic and Transport Properties-REFPROP, Version 10.0, National Institute of Standards and Technology. https://doi.org/10.18434/T4/1502528, https://www.nist.gov/srd/refprop

Liang T, Vecchi A, Knobloch K, Sciacovelli A, Engelbrecht K, Li Y, Ding Y (2022) Key components for Carnot Battery: Technology review, technical barriers and selection criteria. Renew Sustain Energy Rev 163:112478. https://doi.org/10.1016/j.rser.2022.112478

Locatelli M, Schoen F (2013) Global optimization: Theory, algorithms, and applications, MOS-SIAM series on optimization, vol 15. Mathematical Optimization Society and SIAM Philadelphia Pa. https://doi.org/10.1137/1.9781611972672

Ma Z, Albert M, Bao H, Roskilly AP (2022) Pumped thermal energy storage. In: Storing Energy, Elsevier, pp 487–502, https://doi.org/10.1016/b978-0-12-824510-1.00027-1

McBride K, Sundmacher K (2019) Overview of Surrogate Modeling in Chemical Process Engineering. Chem-Ing-Tech 91(3):228–239. https://doi.org/10.1002/cite.201800091https://onlinelibrary.wiley.com/doi/full/10.1002/cite.201800091?saml_referrer

McCormick GP (1976) Computability of global solutions to factorable nonconvex programs: Part i – convex underestimating problems. Math Program 10(1):147–175. https://doi.org/10.1007/BF01580665https://link.springer.com/article/10.1007/BF01580665

McTigue JD, White AJ, Markides CN (2015) Parametric studies and optimisation of pumped thermal electricity storage. Appl Energ 137:800–811. https://doi.org/10.1016/j.apenergy.2014.08.039

McTigue JD, Farres-Antunez P, Ellingwood K, Neises T, White A (2020) Pumped thermal electricity storage with supercritical CO2 cycles and solar heat input. In: THE VII INTERNATIONAL YOUNG RESEARCHERS' CONFERENCE – PHYSICS, TECHNOLOGY, INNOVATIONS (PTI-2020), AIP Publishing, https://doi.org/10.1063/5.0032337

Morandin M, Mercangöz M, Hemrle J, Maréchal F, Favrat D (2013) Thermoeconomic design optimization of a thermo-electric energy storage system based on transcritical CO2 cycles. Energy 58:571–587. https://doi.org/10.1016/j.energy.2013.05.038

Najman J, Bongartz D, Mitsos A (2021) Linearization of McCormick relaxations and hybridization with the auxiliary variable method. J Global Optim 80(4):731–756. https://doi.org/10.1007/s10898-020-00977-xhttps://link.springer.com/article/10.1007/s10898-020-00977-x

Novotny V, Basta V, Smola P, Spale J (2022) Review of Carnot Battery Technology Commercial Development. Energies 15(2):647. https://doi.org/10.3390/en15020647

Palacios A, Elena Navarro M, Barreneche C, Ding Y (2020) Hybrid 3 in 1 thermal energy storage system - Outlook for a novel storage strategy. Appl Energ 274:115024. https://doi.org/10.1016/j.apenergy.2020.115024https://www.sciencedirect.com/science/article/pii/S0306261920305365

Pistikopoulos EN, Tian Y (2024) Advanced Modeling and Optimization Strategies for Process Synthesis. Annu Rev Chem Biomol Eng 15(1):81–103. https://doi.org/10.1146/annurev-chembioeng-100522-112139https://pubmed.ncbi.nlm.nih.gov/38594946/

Psichogios DC, Ungar LH (1992) A hybrid neural network-first principles approach to process modeling. AIChE J 38(10):1499–1511. https://doi.org/10.1002/aic.690381003https://aiche.onlinelibrary.wiley.com/doi/10.1002/aic.690381003

Sanz Garcia L, Jacquemoud E, Jenny P (2019) Thermo-economic heat exchanger optimization for Electro-Thermal Energy Storage based on transcritical CO2 cycles. Conference Proceedings of the European sCO2 Conference, 3rd European Conference on Supercritical CO2 (sCO2) Power Systems 2019: 19th-20th September 2019 p 353, https://doi.org/10.17185/DUEPUBLICO/48917

Schweidtmann AM, Mitsos A (2018) Deterministic Global Optimization with Artificial Neural Networks Embedded. J Optim Theory Appl 189:925–948. https://doi.org/10.1007/s10957-018-1396-0

Schweidtmann AM, Huster WR, Lüthje JT, Mitsos A (2019) Deterministic Global Process Optimization: Accurate (single-species) Properties Via Artificial Neural Networks. Comput Chem Eng 121:67–74. https://doi.org/10.1016/j.compchemeng.2018.10.007

Schweidtmann AM, Netze L, Mitsos A (2020) MeLOn - Machine Learning Models for Optimization. https://git.rwth-aachen.de/avt-svt/public/MeLOn, https://git.rwth-aachen.de/avt-svt/public/MeLOn

Steinmann WD (2014) The CHEST (Compressed Heat Energy STorage) concept for facility scale thermo mechanical energy storage. Energy 69:543–552. https://doi.org/10.1016/j.energy.2014.03.049https://www.sciencedirect.com/science/article/pii/S0360544214003132

Tillmanns D, Pell D, Schilling J, Bardow A (2022) The Thermo-Economic Potential of ORC-Based Pumped-Thermal Electricity Storage: Insights from the Integrated Design of Processes and Working Fluids. Energy Technol 10(7):2200182. https://doi.org/10.1002/ente.202200182https://onlinelibrary.wiley.com/doi/10.1002/ente.202200182

Vecchi A, Knobloch K, Liang T, Kildahl H, Sciacovelli A, Engelbrecht K, Li Y, Ding Y (2022) Carnot Battery development: A review on system performance, applications and commercial state-of-the-art. J Energy Storage 55:105782. https://doi.org/10.1016/j.est.2022.105782

White A, Parks G, Markides CN (2013) Thermodynamic analysis of pumped thermal electricity storage. Appl Therm Eng 53(2):291–298. https://doi.org/10.1016/j.applthermaleng.2012.03.030

Winz J, Nentwich C, Engell S (2021) Surrogate Modeling of Thermodynamic Equilibria: Applications. Sampling and Optimization Chem-ing-tech 93(12):1898–1906. https://doi.org/10.1002/cite.202100092https://onlinelibrary.wiley.com/doi/10.1002/cite.202100092

Zhang S, Campos JS, Feldmann C, Sandfort F, Mathea M, Misener R (2024) Augmenting optimization-based molecular design with graph neural networks. Comput Chem Eng 186:108684. https://doi.org/10.1016/j.compchemeng.2024.108684https://www.sciencedirect.com/science/article/pii/S0098135424001029

Publisher's Note Springer Nature remains neutral with regard to jurisdictional claims in published maps and institutional affiliations.